Co-regulating many properties by co-adjusting few ion channels increases ion channel correlations and the risk of regulation failure

Jane Yang[1,2], Husain Shakil[1,3§], Stéphanie Ratté[1], Steven A. Prescott[1-3†]

[1]Neurosciences and Mental Health, The Hospital for Sick Children, Toronto, Canada
[2]Institute of Biomedical Engineering, University of Toronto, Toronto, Canada
[3]Department of Physiology, University of Toronto, Toronto, Canada

[§]Current affiliation: Division of Neurosurgery, Department of Surgery, University of Toronto, Toronto, Canada

[†]To whom correspondence should be addressed:
Steven A. Prescott
The Hospital for Sick Children
686 Bay St, Toronto, ON, Canada, M5G 0A4
steve.prescott@sickkids.ca

ABSTRACT

Neurons regulate their excitability by adjusting their ion channel levels. Degeneracy – achieving equivalent outcomes (excitability) using different solutions (channel combinations) – facilitates this regulation by enabling a disruptive change in one channel to be offset by compensatory changes in other channels. But neurons must co-regulate many properties. Pleiotropy – the impact of one channel on >1 property – complicates regulation by causing a compensatory change that restores one property to its target value to often disrupt other properties. How then does a neuron simultaneously regulate multiple properties? Here we demonstrate that of the many channel combinations producing the target value for one property (the single-output solution set), few combinations produce the target value for other properties. Combinations producing the target value for two or more properties (the multi-output solution set) correspond to the intersection between single-output solution sets. Properties can be effectively co-regulated only if the number of adjustable channels (n_{in}) exceed the number of regulated properties (n_{out}). Ion channel correlations emerge during homeostatic regulation when the dimensionality of solution space ($n_{in} - n_{out}$) is low. Furthermore, even if each property can be regulated to its target value when considered in isolation, regulation as a whole fails if single-output solution sets do not intersect.

Keywords: Excitability, homeostasis, regulation, degeneracy, neuron, ion channel

INTRODUCTION

Neurons maintain their average firing rate near a target value, or set point, by adjusting their intrinsic excitability and synaptic weights[1-6]. Homeostatic regulation of intrinsic excitability is achieved through feedback control of diverse ion channels[1, 2, 4, 7]. Computational models have successfully employed negative feedback to adjust ion channel densities[8-12] and control theory provides a valuable framework to conceptualize how this occurs[13]. But most of the mechanistic details remain unclear[14, 15] and are not straightforward; for instance, different perturbations can trigger similar changes in excitability via different signaling pathways affecting different ion channels[16], or via different combinations of excitability changes and synaptic scaling[17].

Firing rate homeostasis is facilitated by the ability of different ion channel combinations to produce equivalent excitability[18]. The ability of distinct elements to produce the same outcome is known as degeneracy[19] and has attracted increasing attention in neuroscience[18, 20-27]. Many aspects of neural function at the genetic[28, 29], synaptic[30, 31], cellular[32-39], and network[40-44] levels are now recognized as being degenerate. Ion channel degeneracy facilitates robust homeostatic regulation of neuronal excitability by enabling a disruptive change in one ion channel to be offset by compensatory changes in other ion channels[22, 34, 35, 45-50].

But to maintain good neural coding, neurons must regulate various aspects of their activity beyond average firing rate[51], and must do so while also regulating their energy usage, osmolarity, pH, protein levels, etc.[52-54]. These other cellular properties affect and are affected by neuronal activity (e.g. manipulating metabolic processes can change the firing rate set point[55]), which is to say that properties are not regulated in isolation from one another. And just as each property depends on multiple ion channels, each ion channel can affect multiple properties[38]. This pleiotropy or functional overlap[56] confounds the independent regulation of each property. In response to a perturbation, a compensatory ion channel change that restores one property to its target value may exacerbate rather than mitigate the disturbance of a second property (**Fig. 1A**). In theory, both properties could be regulated by adjusting two or more ion channels (**Fig. 1B**), but this suggests that a small number of ion channels cannot, despite their pleiotropy, regulate many properties simultaneously.

To identify the requirements for simultaneously regulating many properties, we began with experiments to confirm that regulating one property by adjusting a single channel is liable to disrupt other properties. We then proceeded with modeling to unravel how multiple channels must be co-adjusted to ensure proper regulation of >1 property. Our results show that the number of adjustable ion channels (n_{in}) must exceed the number of regulated properties (n_{out}). To some degree this is already known[11, 50, 57] but the implications for homeostatic regulation have not been explored. To that end, we show that the dimensionality of solution space ($n_{in} - n_{out}$) can explain the emergence of ion channel correlations and, importantly, that such correlations presage regulation failure. Overall, we show that feedback mechanisms can maintain multiple properties at their target values by co-adjusting multiple ion channels, but more channels are required than one might expect.

RESULTS

Adjusting an ion channel to regulate one property risks disrupting other properties – experiments

To test experimentally if regulating one property by adjusting one ion channel is liable to disrupt a second property, we disrupted the firing rate of a CA1 pyramidal neuron by blocking its M-type K^+ current (I_M) and then we restored firing rate to its baseline value by inserting a virtual AHP-type K^+ current (I_{AHP}) using dynamic clamp, while also monitoring the firing pattern. Specifically, a neuron was stimulated by injecting irregularly fluctuating (noisy) current under four conditions (**Fig. 2A**): at baseline (blue), after blocking native I_M (black), and again after introducing virtual I_M (cyan) or virtual I_{AHP} (red). Adding virtual I_M was simply to demonstrate that we can replace a native current with an equivalent virtual current. Compensation was modeled by inserting a distinct current with functional overlap, namely I_{AHP} (see Fig. 1). Inserting either virtual I_M or virtual I_{AHP} reversed the increased firing rate, chronic depolarization and attenuated spike height caused by blocking native I_M (**Fig. 2B**). But whereas replacing native I_M with virtual I_M did not affect firing pattern, quantified as the coefficient of variation of the interspike interval (CV_{ISI}), virtual I_{AHP} reduced CV_{ISI} (**Fig. 2C**), often causing the neuron to spike at different times (in response to different stimulus fluctuations) than the neuron with native or virtual I_M (**Fig. 2D**). In other words, as predicted, compensatory "upregulation" of I_{AHP} restored firing rate but disrupted the firing pattern.

Few of the ion channel combinations producing the target value for one property also produce the target value for a second property

We proceeded with computational modeling to identify the conditions required to co-regulate multiple properties. For our investigation, it was critical to account for all the ion channels that are changing. Even for well characterized neurons like pyramidal cells, it is not fully understood which properties are regulated and by which ion channels. Therefore, we built a generic model neuron in which multiple properties are regulated by adjusting a small number of pleiotropic ion channels. The relative rates at which ion channel densities are updated using the "error" in each property differ across properties, consistent with the use of different feedback signals. We focused on independent properties like firing rate and energy efficiency per spike – instead of energy consumption rate, for example, which depends on firing rate – but our conclusions do not hinge on which properties are considered. Target values were chosen arbitrarily.

Simulations were conducted in a single-compartment model neuron whose spikes are generated by a fast sodium conductance and a delayed rectifier potassium conductance with fixed densities. A spike-dependent adaptation mechanism, g_{AHP} was included at a fixed density. Densities of all other channels were either systematically varied (and values producing the target output were selected) or they were adjusted via negative feedback to produce the target output (see Methods). The former approach, which amounts to a grid search, identifies all density combinations producing a target output (i.e. the solution set). The latter approach finds a subset of those combinations through a biologically plausible homeostatic regulation mechanism. Ion channels with adjustable densities included a generic sodium conductance (g_{Na}) and potassium conductance (g_{K}) that both activate with kinetics similar to the delayed rectifier channel, a slower-activating M-type potassium conductance (g_{M}), and a leak conductance (g_{leak}).

We began by testing whether ion channel density combinations that produce the target value for one property also produce a consistent value for other properties. **Figure 3A** shows rheobase for different combinations of $\bar{g}_{\mathrm{Na}}$ and $\bar{g}_{\mathrm{K}}$. The contour from point *a* ($\bar{g}_{\mathrm{Na}}$ = 1.54 mS/cm^2, $\bar{g}_{\mathrm{K}}$ = 0 mS/cm^2) to point *b* ($\bar{g}_{\mathrm{Na}}$ = 4 mS/cm^2, $\bar{g}_{\mathrm{K}}$ = 2.95 mS/cm^2) represents all combinations (i.e. the solution set) yielding a rheobase of 30 μA/cm^2. Despite yielding the same rheobase, density combinations along the *a*-*b* contour did not yield the same minimum sustainable firing rate (f_{min}) (**Fig. 3B**). The value of f_{min} reflects spike initiation dynamics: f_{min} >>0 spk/s is consistent with class 2 excitability[58] and operation as a coincidence detector[59], whereas $f_{\mathrm{min}} \approx 0$ spk/s is consistent with class 1 excitability and operation as an integrator, with several consequences (**Fig. S1**). After adding g_{AHP} to expand the stimulus range over which fluctuation-driven spikes occur, we plotted the firing rate driven by irregularly fluctuating (noisy) I_{stim} for different combinations of $\bar{g}_{\mathrm{Na}}$ and $\bar{g}_{\mathrm{K}}$ (**Fig. 3C**). Density combinations yielding the same rheobase did not yield equivalent stimulation-evoked firing rates (**Fig. 3D**).

Having demonstrated that ion channel density combinations yielding the target value for one aspect of excitability (e.g. rheobase) yield differing values for other aspects of excitability (e.g. f_{min} or firing rate), we predicted that the same lack of generalization would extend to other cellular properties (e.g. energy efficiency). Spikes are energetically costly[60] but vary in their energetic efficiency based on the temporal overlap in sodium and potassium channel activation[61] (**Fig. S2**). Using responses reported in Figure 3C, we measured energy consumption rate for combinations of

$\bar{g}_{\mathrm{Na}}$ and $\bar{g}_{\mathrm{K}}$ (**Fig. 3E**). Energy consumption rate increased with firing rate, as expected, but did not increase equivalently across all density combinations, as evident from the variation in energy consumption rate along the iso-firing rate contour (**Fig. 3F**). This is due to differences in energy efficiency (**Fig. 3G**) determined as the energy consumed per spike relative to the theoretical minimum (see Methods). Density combinations yielding equally efficient spikes yielded different stimulation-evoked firing rates and rheobase values (**Fig. 3H**). One might presume that spikes are produced as efficiently as possible and that energy efficiency is maintained above a lower bound rather than being regulated to a specific value, but energy efficiency decreases propagation safety factor[62] and a target value likely emerges by balancing these competing interests[63].

Adjusting an ion channel to regulate one property risks disrupting other properties – simulations

Like experiments in Figure 2, we tested if restoring firing rate to its target value via compensatory changes in either of two ion channels (**Fig. 4A**) after perturbing a third channel would differentially affect energy efficiency in our model neuron. Grey circles on **Figure 4B** show randomly chosen combinations of $\bar{g}_{\mathrm{Na}}$ and $\bar{g}_{\mathrm{leak}}$ that yield a firing rate of 40 spk/s when $\bar{g}_{\mathrm{K}}$ = 2 mS/cm^2. When $\bar{g}_{\mathrm{K}}$ was "blocked" (abruptly reset to 0 mS/cm^2), firing rate jumped to ~93 spk/s before being restored to 40 spk/s via feedback control of either $\bar{g}_{\mathrm{Na}}$ (pink) or $\bar{g}_{\mathrm{leak}}$ (cyan) (**Fig. 4C**). As $\bar{g}_{\mathrm{Na}}$ or $\bar{g}_{\mathrm{leak}}$ converged on new, compensated densities, firing rate returned to its target value but energy efficiency was affected in opposite ways (**Fig. 4D**). If energy efficiency is also regulated, then $\bar{g}_{\mathrm{Na}}$ or $\bar{g}_{\mathrm{leak}}$ must be co-adjusted (see Fig. 1B) in a way that restores firing rate without disrupting energy efficiency.

Geometrical explanation for the relationship between single- and multi-output solutions

Next, we sought a geometrical explanation for how to co-adjust >1 ion channel in order to co-regulate >1 property. The left panel of **Figure 5A** shows all combinations of $\bar{g}_{\mathrm{Na}}$ and $\bar{g}_{\mathrm{K}}$ (n_{in} = 2) yielding the target value for firing rate (red) *or* energy efficiency (green) (n_{out} = 1). Like in Figures 3 and 4, the solution set for each property corresponds to a curve. The multi-output solution set for firing rate *and* energy efficiency (n_{out} = 2) corresponds to where the two single-output solution sets intersect, which occurs at a point – only one density combination yields the target values for both properties, meaning the multi-output solution is unique. But if another conductance like g_{leak} is adjustable (n_{in} = 3), the curves in 2D parameter space (left panel) transform into surfaces in 3D parameter space

(right panel) and those surfaces intersect along a curve – many density combinations yield the target values for both properties, meaning the multi-output solution is degenerate. The same patterns are evident for firing rate *and* input resistance (**Fig. 5B**) or energy efficiency *and* input resistance (**Fig. 5C**). **Figure 5D** shows that if all three properties – firing rate, energy efficiency *and* input resistance – are regulated (n_{out} = 3), the multi-output solution set is empty for n_{in} = 2 (i.e. the three curves do not intersect at a common point [left panel] unless $\bar{g}_{\mathrm{leak}}$ is reset to 1.95 mS/cm^2 [inset]) and is unique for n_{in} = 3 (right panel). From this, we conclude that robust regulation of *n* properties requires >*n* adjustable ion channels even if each ion channel contributes to regulation of >1 property. This is like a system of linear equations, which is said to be *underdetermined* if there are fewer equations (outputs) than unknowns (inputs) (see Discussion).

In all simulations involving homeostatic regulation, properties were regulated to within certain bounds of the target rather than to a precise value, despite how solution sets are depicted. When tolerances are depicted, single-output solution sets correspond to thin strips (rather than curves) or shallow volumes (rather than surfaces) in 2D and 3D parameter space, respectively (**Fig. S3**). The width, depth, etc. are proportional to the tolerance. How does this impact multi-output solutions? *Thin* 2D strips intersect at a small patch (unlike curves intersecting at a point) but that patch in 2D parameter space (**Fig. S3A**) is unlike the long 1D curve formed by *broad* 2D surfaces intersecting in 3D parameter space (cf. right panels of Fig. 4). Likewise, *shallow* 3D volumes intersect at a narrow tube (unlike surfaces intersecting at a curve) but that tube in 3D parameter space (**Fig. S3B**) is unlike the broad 2D surface formed by *deep* 3D volumes intersecting in 4D parameter space. In other words, increasing tolerance does not expand solution space dimensionality the same way as increasing n_{in}. That said, if a property is maintained above or below some bound (see Fig. 9), the solution space is higher dimensional than for regulation to a target value under otherwise equivalent conditions.

The dimensionality of solution space affects ion channel correlations

We predicted that the dimensionality of solution space – point (0D), curve (1D), surface (2D), volume (3D), etc. – affects ion channel correlations by limiting the degrees of freedom. To explore this, we measured ion channel correlations within single- and multi-output solution sets found through homeostatic regulation. **Figure 6A** shows all combinations of $\bar{g}_{\mathrm{Na}}$ and $\bar{g}_{\mathrm{K}}$ (n_{in} = 2) producing the target firing rate (n_{out} = 1). Correlation between $\bar{g}_{\mathrm{Na}}$ and $\bar{g}_{\mathrm{K}}$ is high because

homeostatically determined solutions are constrained to fall along a curve; under those conditions, variation in one channel is offset solely by variation in the other channel, and all covariance is thus captured in a single pairwise relationship. If $\bar{g}_{\mathrm{M}}$ is also allowed to vary (n_{in} = 3), homeostatically determined solutions spread across a surface and pairwise correlations become predictably weaker (**Fig. 6B**) since variation in one channel can be offset by variation in two other channels, and covariance is diluted across >1 pairwise relationship. If additional channels are allowed to vary ($n_{\mathrm{in}} \geq 4$), solutions distribute over higher-dimensional manifolds and pairwise correlations further weaken (**Fig. 6C**). However, if firing rate *and* energy efficiency are both regulated ($n_{\mathrm{out}} = 2$; **Fig. 6D**), homeostatically determined solutions are once again constrained to fall along a curve when $n_{\mathrm{in}} = 3$, and pairwise correlations strengthen (**Fig. 6E**). Increasing n_{in} to 4 while keeping n_{out} at 2 caused correlations to weaken (**Fig. 6F**). These results confirm the predicted impact of solution space dimensionality on ion channel correlations.

O'Leary et al.[64] demonstrated how the relative rates at which different ion channel densities are controlled impact their correlation. This is reproduced in **Figure 7A**, where, from the same initial conditions (density combinations), homeostatic control with different relative rates (shown in pink and cyan) produce solutions with different correlations. Relative control rates can affect not only the strength of pairwise correlations, but also the sign (compare correlation between $\bar{g}_{\mathrm{Na}}$ and $\bar{g}_{\mathrm{M}}$). However, if firing rate *and* energy efficiency are both homeostatically regulated, correlations strengthen (consistent with results from Fig. 6) and become independent of the relative control rates because solutions are limited to a lower-dimensional solution space (**Fig. 7B**). Recall that dimensionality of the multi-output solution set corresponds to $n_{\mathrm{in}} - n_{\mathrm{out}}$. For relative control rates to influence ion channel correlations, homeostatically determined solutions must fall on a solution space with dimensionality >1, but not >>1 lest pairwise correlations be diluted.

The dimensionality of solution space also affects the success of homeostatic regulation

Beyond affecting the ion channel correlations that emerge through homeostatic regulation, we predicted that the dimensionality of solution space affects whether multiple properties can be successfully regulated to their target values. **Figure 8A** shows an example in which control of $\bar{g}_{\mathrm{Na}}$, $\bar{g}_{\mathrm{K}}$, and $\bar{g}_{\mathrm{M}}$ successfully regulates firing rate. **Figure 8B** shows successful regulation of energy efficiency via control of the same three channels. Using the same initial conditions and relative

control rates, the system failed to co-regulate firing rate *and* energy efficiency (**Fig. 8C**). Notably, coordinated regulation of both properties was achieved using other relative control rates (see Figs. 6C and 7B) or using the same relative rates but starting from different initial conditions (not shown), suggesting that low-dimensional solutions are less 'accessible' (i.e. a smaller set of relative control rates succeed in finding the solution space).

Figure 9 shows additional examples in which control of $\bar{g}_{\mathrm{Na}}$, $\bar{g}_{\mathrm{K}}$, and $\bar{g}_{\mathrm{M}}$ regulates firing rate and energy efficiency. In these simulations, firing rate is regulated to a precise target value whereas energy efficiency is maintained above a lower bound; the single-output solution set for energy efficiency thus corresponds to a volume rather than a surface for $n_{\mathrm{in}} = 3$. For energy efficiency ≥22%, homeostatically determined solutions converge on the iso-firing rate surface without regulation of energy efficiency having much effect (**Fig. 9A**). For energy efficiency ≥27%, solutions initially converge onto part of the iso-firing rate surface that sits outside the targeted energy efficiency volume, but without energy efficiency requirements being met, solutions then move across the surface until reaching the intersection with the energy efficiency volume (**Fig. 9B**). By converging on the intersection, which is a curve, ion channel correlations are stronger than in Figure 9A. For energy efficiency ≥30%, the iso-firing rate surface and targeted energy efficiency volume do not intersect and solutions thus proceed to a point between the two single-output solution sets constrained by $\bar{g}_{\mathrm{K}}$ and $\bar{g}_{\mathrm{M}}$ reaching 0 mS/cm^2 (**Fig. 9C**). In this last example, neither property is optimally regulated but the outcome is a reasonable compromise. In other scenarios, regulation might have failed outright if, in the absence of an upper bound, for example, the ion channel densities continued to increase without properties ever reaching their target values. This highlights that co-regulation of multiple properties might fail (or find sub-optimal solutions) not because single-output solutions do not exist, but because even large single-output solution sets might not intersect, meaning no multi-output solution exists.

DISCUSSION

This study has explored how neurons manage to co-regulate >1 property by co-adjusting >1 ion channel. Being able to produce the same output using diverse ion channel combinations is key insofar as this degeneracy allows solution sets to be large. But of the many ion channel combinations that produce the desired output for one property, few also produce the desired output for other

properties (Fig. 3); consequently, ion channel adjustments that regulate one property are liable to disrupt other properties (Figs. 2 and 4). The multi-output solution set corresponds to the intersection between single-output solution sets (Fig. 5), meaning ion channels must be co-adjusted to remain within the more restricted multi-output solution space. The dimensionality of solution space corresponds to the difference between the number of adjustable ion channels (n_{in}) and the number of regulated outputs (n_{out}). Coordinated regulation of n properties requires at least n adjustable ion channels for a unique solution, and at least $n+1$ channels for a degenerate solution. Ion channel pleiotropy (i.e. reusing the same channel to regulate >1 property) does not enable more properties to be regulated using fewer channels.

A direct analogy can be made with a system of linear equations. Each unknown constitutes a degree of freedom and each equation constitutes a constraint that reduces the degrees of freedom by one. The system is said to be overdetermined if equations outnumber unknowns, and under-determined if unknowns outnumber equations. An underdetermined system can have infinite solutions. Degeneracy is synonymous with underdetermination, which highlights that degeneracy depends not only on ion channel diversity, but also on those channels not having to co-regulate "too many" properties. Extra degrees of freedom broaden the range of available solutions, meaning a good solution is liable to exist over a broader range of conditions. On the other hand, if constraints outnumber the degrees of freedom, the system becomes overdetermined and solutions disappear (e.g. Fig. 4D), which can cause regulation to fail (see below). One might reasonably speculate that ion channel diversity has been selected for because it enables the addition of new functionality (e.g. excitability) while keeping the cell underdetermined, lest pre-existing functions (e.g. osmoregulation) be disrupted.

There are notable similarities and differences between a neuron adjusting its ion channel densities to regulate properties and a scientist trying to infer conductance densities based on the measured values of those properties (i.e. fitting a model to experimental data). Fitting a model with n parameters to many outputs (e.g. firing rate *and* input resistance *and* rheobase *and* spike height) is more difficult but yields better parameter estimates than fitting the same model to just one output[57], just as regulating more properties makes a multi-output solution set smaller. But how good are those parameter estimates? Can one confidently infer the true conductance densities in a particular neuron by measuring and fitting enough properties? Degeneracy makes solving this

inverse problem difficult, if not impossible[65]. The neuron solves the forward problem, producing a firing rate, input resistance, etc. based on its ion channel density combination. That combination is determined by negative feedback, but the precise densities are unimportant so long as the combination produces the target values for all regulated properties (which will happen for each and every density combination within the multi-output solution set). As conditions change, the multi-output solution will evolve and negative feedback will adjust densities accordingly. A neuron needs to regulate its properties but does not do so by regulating its conductance densities to particular values; in that respect, a neuron does not solve an inverse problem. Moreover, neurons have evolved under selective pressure to be degenerate (see above), not parsimonious, contrary to how scientists typically construct their models.

Previous studies using grid searches to explore degeneracy have tended to apply selection criteria simultaneously, finding the "multi-output" solution set in one fell swoop. In contrast, we considered one criterion (property) at a time in order to find each single-output solution set, which we then combined to find the multi-output solution. The former approach is akin to aggregating several error functions to create a single-objective problem, whereas the latter resembles multi-objective optimization. Nevertheless, past studies have observed that certain parameter changes (in a particular direction through parameter space) dramatically affect some properties but not others[34, 66], consistent with manifolds representing the single-output solution sets for sensitive and insensitive properties lying orthogonal to one another in parameter space. The effects of solution dimensionality on ion channel correlations and regulation failure (see below) highlight the value of a multi-objective perspective, which implicitly recognizes that there are multiple properties, each with its own feedback loop, even if those feedback loops are inter-connected by the control of overlapping ion channels. Our results show that co-regulating many properties using a common set of ion channels is feasible only if enough *different* channels are involved. Indeed, for co-adjustments to work, channels must differ from each other in how they affect each property, which emphasizes the distinction between degeneracy and redundancy.

Ion channel correlations have been studied using both simulations[8, 30, 33, 37, 64, 67-69] and experiments[47, 70-74]. These correlations have been ascribed to the co-regulation of ion channels. The relative rates with which different conductance densities are controlled dictate the direction in which trajectories move through parameter space, which in turn dictates how trajectories approach

and distribute across the solution manifold[64]. Our results are consistent with that explanation (Fig. 7) but also highlight the importance of manifold dimensionality (Fig. 6). Correlations are stronger (but less sensitive to relative control rates) if trajectories reach a 1D manifold (curve) than if they reach a 2D manifold (surface). Pairwise correlations are even weaker if the manifold is higher-dimensional (volume, etc.). Existence of pairwise correlations thus suggests that the dimensionality of solution space (= $n_{in} - n_{out}$) is relatively low. This may be surprising since n_{in} is high, but makes sense if n_{out} is also high; in other words, there are *many* channels, but they are responsible for regulating *many* properties. In reality, n_{out} is constrained by n_{in}, but neurons might take advantage of regulating as many properties as their ion channel diversity safely allows, leading to a relatively low dimensional solution space.

Homeostatic regulation can fail for different reasons. If there are no solutions (i.e. the solution set is empty), negative feedback cannot regulate properties to their target values. A multi-output solution set can be empty because single-output solution sets do not intersect (Fig. 9C), meaning regulation of different properties to their respective target values is incompatible. This is distinct from a single-output solution set being empty, which means regulation of a particular property is impossible. Regulation can also fail because negative feedback fails to converge on available solutions (Fig. 8C). Notably, a multi-output solution set may become less 'accessible' (lower dimensional) as single-output solution sets start to separate (Fig. 9B), and may foreshadow the eventual disjunction of those solution sets (Fig. 9C). Regulation can also fail because feedback signaling is compromised. These failure modes are not mutually exclusive; for example, a system might reach less 'accessible' solutions if control rates are normally flexible, but might fail to reach those solutions if control rate flexibility is reduced. Failed homeostatic regulation may have similar consequence regardless of how the failure occurs, consistent with the emergence of common disease phenotypes despite vastly different underlying pathologies[75]. That said, subtle differences in exactly how the failure transpires may provide important clues to help pinpoint the underlying mechanism(s).

In conclusion, neurons manage to homeostatically regulate multiple properties by co-adjusting pleiotropic ion channels. Despite reusing the same channels to regulate different properties, many channels are required to simultaneously regulate many properties, which may account for why evolution has yielded such diverse channels and why their transcriptional

regulation has become so complicated[76]. Given how difficult it is to study regulation of any one property, studying the coordinated regulation of multiple properties is truly daunting. Theory and modeling are thus critical for uncovering general principles[8, 77] to ensure continued progress.

METHODS

Slice electrophysiology. All procedures were approved by the Hospital for Sick Children Animal Care Committee. Using the same procedures and equipment previously described[78], coronal slices of hippocampus were prepared from an adult mouse and a CA1 pyramidal neuron was recorded using whole-cell patch clamp. A noisy stimulus was generated through an Ornstein-Uhlenbeck process (see Eqn 7) with τ_{stim} = 5 ms, μ_{stim} = 60 pA, and σ_{stim} = 10 pA; the same stimulus was re-played on each trial. Native I_{M} was blocked by bath application of 10 uM XE991 (Tocris). The block was continued throughout dynamic clamp experiments. Virtual I_{M} and I_{AHP} were modeled as per Eqn 6 (with τ_{q} = 100 ms, β_{q} = -35 mV and γ_{q} = 4 mV for I_{M}, and τ_{p} = 600 ms, β_{p} = 0 mV and γ_{p} = 1 mV for I_{AHP}) and were applied using the dynamic clamp capabilities of Signal v6 (Cambridge Electronic Design). The density of each virtual conductance was adjusted to produce the desired firing rates ($\bar{g}_{\text{M}}$ = 10 nS, $\bar{g}_{\text{AHP}}$ = 120-150 nS).

Neuron model. Our base model includes a fast-activating sodium conductance (g_{fast}) and a slower-activating potassium conductance (g_{slow}) which together are sufficient to produce spikes. Other conductances were added to modulate excitability.

$$C\frac{dV}{dt} = I_{\text{stim}} - \bar{g}_{\text{fast}} m_{\infty}(V)(V - E_{\text{Na}}) - \bar{g}_{\text{slow}} w(V - E_{\text{K}}) - \bar{g}_{\text{Na}} n(V - E_{\text{Na}}) - \bar{g}_{\text{K}} n(V - E_{\text{K}}) - \bar{g}_{\text{AHP}} p(V - E_{\text{K}}) - \bar{g}_{\text{M}} q(V - E_{\text{K}}) - \bar{g}_{\text{leak}}(V - E_{\text{L}}), \quad \text{(Eqn 1)}$$

where V is voltage and m changes instantaneously with V whereas other gating variables change more slowly. The spike-generating conductances g_{fast} and g_{slow} were modeled using a Morris-Lecar formalism[45], with C= 2 μF/cm^2, E_{Na}= 50 mV, E_{K}= -100 mV, E_{leak}= -70 mV, φ_{w}= 0.15, $\bar{g}_{\text{fast}}$= 20 mS/cm^2, $\bar{g}_{\text{slow}}$= 20 mS/cm^2, $\bar{g}_{\text{leak}}$= 2 mS/cm^2, β_{m}= -1.2 mV, γ_{m}= 18 mV, β_{w} = -10 mV, and γ_{w}= 10 mV. A generic sodium conductance (g_{Na}) and potassium conductance (g_{K}) were modeled using Hodgkin-Huxley formalism as described by Ratté et al.[35]

$$I_{\text{Na,K}} = \bar{g}_{\text{Na,K}} n\left(V - E_{\text{Na,K}}\right), \quad \text{(Eqn 2)}$$

$$\frac{dn}{dt} = \alpha(1 - n) - \beta n, \quad \text{(Eqn 3)}$$

$$\alpha = \frac{k_\alpha (V - V_\alpha)}{e^{\left(V - \frac{V_\alpha}{s_\alpha}\right)} - 1}, \quad \text{(Eqn 4)}$$

$$\beta = k_\beta e^{\left(V - \frac{V_\alpha}{s_\alpha}\right)}, \quad \text{(Eqn 5)}$$

where $V_{\alpha,\beta}$ = - 24 mV, $s_{\alpha,\beta}$ = - 17 mV, and $k_{\alpha,\beta}$ = 1 ms^{-1}. Note that g_{Na} and g_{K} differ only in their reversal potentials. Channels approximating a calcium-activated potassium conductance (g_{AHP}) and an M-type potassium conductance (g_{M}) were modeled as described by Prescott et al.[79]

$$\frac{dz}{dt} = \left\{ \frac{1}{1 + e^{\left(\frac{\beta_z - V}{\gamma_z}\right)}} - z \right\} / \tau_z, \quad \text{(Eqn 6)}$$

where z stands for p and q, $\tau_{p,q}$= 100 ms, $\gamma_{p,q}$ = 4 mV, β_p = 0 mV and β_q = -35 mV. Maximal conductance densities for g_{leak}, g_{Na}, g_{K} and g_{M} were systematically varied or adjusted by a homeostatic feedback mechanism (see below). Any other parameters that differ from the sources cited above are reported in the relevant figure legends. Injected current I_{stim} was applied as either a constant step or as noisy fluctuations modeled with an Ornstein-Uhlenbeck process

$$\frac{dI_{\mathrm{stim}}}{dt} = \frac{I_{\mathrm{stim}} - \mu_{\mathrm{stim}}}{\tau_{\mathrm{stim}}} + \frac{S\sigma_{\mathrm{stim}}}{\sqrt{dt}} N(t), \quad \text{(Eqn 7)}$$

where τ_{stim} is a time constant that controls the rate at which I_{stim} drifts back towards the mean μ_{stim}, and $N(t)$ is a random number drawn from a normal distribution with 0 mean and unit variance that is scaled by $S\sigma_{\mathrm{stim}}$, where a scaling factor $S = \sqrt{2/\tau_{\mathrm{stim}}}$ makes the standard deviation σ_{stim} independent of τ_{stim}. All simulations were conducted in MATLAB using the forward Euler integration method and a time step of 0.05-0.1 ms.

Energy calculations. Energy consumption rate was calculated as in Hasenstaub et al.[80] Briefly, models were stimulated with a fast fluctuating stimulus (μ_{stim} = 40 μA/cm^2, σ_{stim} = 10 μA/cm^2). Sodium and potassium current through all channels was integrated for 1 second to determine the charge for each ion species, which was then converted to ion flux based on the elementary charge 1.602 x 10^{-19} C. Based on the 3:2 stoichiometry of the Na^+/K^+ pump, we divided the number of sodium and potassium ions by 3 and 2, respectively, and used the maximum of those two values as the energy consumption rate (in ATP/cm^2·s). Energy efficiency was calculated as the ratio between capacitive minimum and total Na^+ flux during an action potential[61]. Briefly, voltage was reset to -40 mV to evoke a single spike in all models. Models were treated as pure capacitors to calculate the minimum capacitive current as $C\Delta V$, where C is the capacitance and ΔV is the difference between the resting membrane potential and the spike peak.

Grid search. Models were tested with conductance density combinations chosen from a 100x100 or 30x30x30 grid for 2D and 3D plots, respectively. To depict each single-output solution set, all models with outputs within a range (tolerance) of the target value (± 3 spk/s for firing rate, ± 0.25 % for energy efficiency, and ± 0.003 $k\Omega \cdot cm^2$ for input resistance) were selected and a curve or surface was fit to those successful models. The same tolerances were implemented in the homeostatic learning rule (see below) to minimize ringing. Tolerances are illustrated in Figure S3 but were not shown in other figures for sake of clarity.

Feedback control. We modified O'leary et al.'s homeostatic learning rule[8, 64] to exclude Ca^{2+} dynamics and use proportional instead of integral error as the feedback signal. Briefly, the error in each output was determined as the difference between the current and target values. For each conductance $\bar{g}_i$, the error was scaled by its regulation rate (τ_i) and added to the conductance (see Fig. 4A). For homeostatic regulation of >1 property, we used the sum of errors to update conductance densities (see Fig. 6D). A single run consists of a maximum of 200 iterations, during which a model must reach and maintain its regulated property within the tolerance for five consecutive iterations. All models that reached that target output(s) did so in well under 100 iterations; models not reaching their target output(s) after 200 iterations were considered to have failed. Conductances during the last five iterations were averaged and reported as the final value. See **Table S1** for the initial conductance values and control rates used for each figure.

CODE AVAILABILITY

All code is available at http://prescottlab.ca/code-for-models and will be made available at GitHub and ModelDB upon publication.

REFERENCES

1. Turrigiano, G., Abbott, L.F. & Marder, E. Activity-dependent changes in the intrinsic properties of cultured neurons. *Science* **264**, 974-977 (1994).
2. O'Leary, T., van Rossum, M.C. & Wyllie, D.J. Homeostasis of intrinsic excitability in hippocampal neurones: dynamics and mechanism of the response to chronic depolarization. *J Physiol* **588**, 157-170 (2010).
3. Aizenman, C.D., Akerman, C.J., Jensen, K.R. & Cline, H.T. Visually driven regulation of intrinsic neuronal excitability improves stimulus detection in vivo. *Neuron* **39**, 831-842 (2003).

4. Desai, N.S., Rutherford, L.C. & Turrigiano, G.G. Plasticity in the intrinsic excitability of cortical pyramidal neurons. *Nat Neurosci* **2**, 515-520 (1999).
5. Hengen, K.B., Lambo, M.E., Van Hooser, S.D., Katz, D.B. & Turrigiano, G.G. Firing rate homeostasis in visual cortex of freely behaving rodents. *Neuron* **80**, 335-342 (2013).
6. van, W.I., van Hooft, J.A. & Wadman, W.J. Background activity regulates excitability of rat hippocampal CA1 pyramidal neurons by adaptation of a K^+ conductance. *J Neurophysiol* **95**, 2007-2012 (2006).
7. Joseph, A. & Turrigiano, G.G. All for one but not one for all: Excitatory synaptic scaling and intrinsic excitability are coregulated by CaMKIV, whereas inhibitory synaptic scaling is under independent control. *J Neurosci* **37**, 6778-6785 (2017).
8. O'Leary, T., Williams, A.H., Franci, A. & Marder, E. Cell types, network homeostasis, and pathological compensation from a biologically plausible ion channel expression model. *Neuron* **82**, 809-821 (2014).
9. O'Leary, T. & Marder, E. Temperature-robust neural function from activity-dependent ion channel regulation. *Curr Biol* **26**, 2935-2941 (2016).
10. Liu, Z., Golowasch, J., Marder, E. & Abbott, L.F. A model neuron with activity-dependent conductances regulated by multiple calcium sensors. *J Neurosci* **18**, 2309-2320 (1998).
11. Olypher, A.V. & Prinz, A.A. Geometry and dynamics of activity-dependent homeostatic regulation in neurons. *J Comput Neurosci* **28**, 361-374 (2010).
12. LeMasson, G., Marder, E. & Abbott, L.F. Activity-dependent regulation of conductances in model neurons. *Science* **259**, 1915-1917 (1993).
13. O'Leary, T. & Wyllie, D.J. Neuronal homeostasis: time for a change? *J Physiol* **589**, 4811-4826 (2011).
14. Davis, G.W. Homeostatic control of neural activity: from phenomenology to molecular design. *Annu Rev Neurosci* **29**, 307-323 (2006).
15. Turrigiano, G. Too many cooks? Intrinsic and synaptic homeostatic mechanisms in cortical circuit refinement. *Annu Rev Neurosci* **34**, 89-103 (2011).
16. Kulik, Y., Jones, R., Moughamian, A.J., Whippen, J. & Davis, G.W. Dual separable feedback systems govern firing rate homeostasis. *Elife* **8**, e45717 (2019).
17. Maffei, A. & Turrigiano, G.G. Multiple modes of network homeostasis in visual cortical layer 2/3. *J Neurosci* **28**, 4377-4384 (2008).
18. Marder, E. Variability, compensation, and modulation in neurons and circuits. *Proc Natl Acad Sci USA* **108 Suppl 3**, 15542-15548 (2011).
19. Edelman, G.M. & Gally, J.A. Degeneracy and complexity in biological systems. *Proc Natl Acad Sci USA* **98**, 13763-13768 (2001).
20. Marder, E. & Goaillard, J.M. Variability, compensation and homeostasis in neuron and network function. *Nat Rev Neurosci* **7**, 563-574 (2006).
21. Cropper, E.C., Dacks, A.M. & Weiss, K.R. Consequences of degeneracy in network function. *Curr Opin Neurobiol* **41**, 62-67 (2016).

22. O'Leary, T. Homeostasis, failure of homeostasis and degenerate ion channel regulation. *Curr Opin Physiol* **2**, 129-138 (2018).
23. Ratté, S. & Prescott, S.A. Afferent hyperexcitability in neuropathic pain and the inconvenient truth about its degeneracy. *Curr Opin Neurobiol* **36**, 31-37 (2016).
24. Tononi, G., Sporns, O. & Edelman, G.M. Measures of degeneracy and redundancy in biological networks. *Proc Natl Acad Sci USA* **96**, 3257-3262 (1999).
25. Goaillard, J.M. & Dufour, M.A. The pros and cons of degeneracy. *Elife* **3**, e02615 (2014).
26. Mason, P.H., Dominguez, D.J., Winter, B. & Grignolio, A. Hidden in plain view: degeneracy in complex systems. *Biosystems* **128**, 1-8 (2015).
27. Rathour, R.K. & Narayanan, R. Degeneracy in hippocampal physiology and plasticity. *Hippocampus* **29**, 980-1022 (2019).
28. Klassen, T.*, et al.* Exome sequencing of ion channel genes reveals complex profiles confounding personal risk assessment in epilepsy. *Cell* **145**, 1036-1048 (2011).
29. Trojanowski, N.F., Padovan-Merhar, O., Raizen, D.M. & Fang-Yen, C. Neural and genetic degeneracy underlies Caenorhabditis elegans feeding behavior. *J Neurophysiol* **112**, 951-961 (2014).
30. Mukunda, C.L. & Narayanan, R. Degeneracy in the regulation of short-term plasticity and synaptic filtering by presynaptic mechanisms. *J Physiol* **595**, 2611-2637 (2016).
31. Anirudhan, A. & Narayanan, R. Analogous synaptic plasticity profiles emerge from disparate channel combinations. *J Neurosci* **35**, 4691-4705 (2015).
32. Kim, E.Z., Vienne, J., Rosbash, M. & Griffith, L.C. Nonreciprocal homeostatic compensation in Drosophila potassium channel mutants. *J Neurophysiol* **117**, 2125-2136 (2017).
33. Taylor, A.L., Goaillard, J.M. & Marder, E. How multiple conductances determine electrophysiological properties in a multicompartment model. *J Neurosci* **29**, 5573-5586 (2009).
34. Drion, G., O'Leary, T. & Marder, E. Ion channel degeneracy enables robust and tunable neuronal firing rates. *Proc Natl Acad Sci USA* **112**, E5361-5370 (2015).
35. Ratté, S., Zhu, Y., Lee, K.Y. & Prescott, S.A. Criticality and degeneracy in injury-induced changes in primary afferent excitability and the implications for neuropathic pain. *Elife* **3**, 02370 (2014).
36. Mittal, D. & Narayanan, R. Degeneracy in the robust expression of spectral selectivity, subthreshold oscillations, and intrinsic excitability of entorhinal stellate cells. *J Neurophysiol* **120**, 576-600 (2018).
37. Jain, A. & Narayanan, R. Degeneracy in the emergence of spike-triggered average of hippocampal pyramidal neurons. *Sci Rep* **10**, 374 (2020).
38. Gunay, C., Edgerton, J.R. & Jaeger, D. Channel density distributions explain spiking variability in the globus pallidus: a combined physiology and computer simulation database approach. *J Neurosci* **28**, 7476-7491 (2008).

39. Migliore, R., *et al.* The physiological variability of channel density in hippocampal CA1 pyramidal cells and interneurons explored using a unified data-driven modeling workflow. *PLoS Comput Biol* **14**, e1006423 (2018).
40. Grashow, R., Brookings, T. & Marder, E. Compensation for variable intrinsic neuronal excitability by circuit-synaptic interactions. *J Neurosci* **30**, 9145-9156 (2010).
41. Marder, E. & Taylor, A.L. Multiple models to capture the variability in biological neurons and networks. *Nat Neurosci* **14**, 133-138 (2011).
42. Prinz, A.A., Bucher, D. & Marder, E. Similar network activity from disparate circuit parameters. *Nat Neurosci* **7**, 1345-1352 (2004).
43. Price, C.J. & Friston, K.J. Degeneracy and cognitive anatomy. *Trends Cog Sci* **6**, 416-421 (2002).
44. Onasch, S. & Gjorgjieva, J. Circuit stability to perturbations reveals hidden variability in the balance of intrinsic and synaptic conductances. *J Neurosci* **40**, 3186-3202 (2020).
45. Rho, Y.A. & Prescott, S.A. Identification of molecular pathologies sufficient to cause neuropathic excitability in primary somatosensory afferents using dynamical systems theory. *PLoS Comput Biol* **8**, e1002524 (2012).
46. Swensen, A.M. & Bean, B.P. Robustness of burst firing in dissociated purkinje neurons with acute or long-term reductions in sodium conductance. *J Neurosci* **25**, 3509-3520 (2005).
47. Zhao, S. & Golowasch, J. Ionic current correlations underlie the global tuning of large numbers of neuronal activity attributes. *J Neurosci* **32**, 13380-13388 (2012).
48. Achard, P. & De Schutter, E. Complex parameter landscape for a complex neuron model. *PLoS Comput Biol* **2**, e94 (2006).
49. Bhalla, U.S. & Bower, J.M. Exploring parameter space in detailed single neuron models: simulations of the mitral and granule cells of the olfactory bulb. *J Neurophysiol* **69**, 1948-1965 (1993).
50. Olypher, A.V. & Calabrese, R.L. Using constraints on neuronal activity to reveal compensatory changes in neuronal parameters. *J Neurophysiol* **98**, 3749-3758 (2007).
51. Stemmler, M. & Koch, C. How voltage-dependent conductances can adapt to maximize the information encoded by neuronal firing rate. *Nat.Neurosci.* **2**, 521-527 (1999).
52. Frere, S. & Slutsky, I. Alzheimer's disease: From firing instability to homeostasis network collapse. *Neuron* **97**, 32-58 (2018).
53. Fisher, S.K., Heacock, A.M., Keep, R.F. & Foster, D.J. Receptor regulation of osmolyte homeostasis in neural cells. *J Physiol* **588**, 3355-3364 (2010).
54. Balch, W.E., Morimoto, R.I., Dillin, A. & Kelly, J.W. Adapting proteostasis for disease intervention. *Science* **319**, 916-919 (2008).
55. Styr, B., *et al.* Mitochondrial regulation of the hippocampal firing rate set point and seizure susceptibility. *Neuron* **102**, 1009-1024.e1008 (2019).
56. Goaillard, J.M. & Marder, E. Ion channel degeneracy, variability, and covariation in neuron and circuit resilience. *Annu Rev Neurosci* (in press).

57. Foster, W.R., Ungar, L.H. & Schwaber, J.S. Significance of conductances in Hodgkin-Huxley models. *J Neurophysiol* **70**, 2502-2518 (1993).
58. Hodgkin, A.L. The local electric changes associated with repetitive action in a non-medullated axon. *J Physiol* **107**, 165-181 (1948).
59. Ratté, S., Lankarany, M., Rho, Y.A., Patterson, A. & Prescott, S.A. Subthreshold membrane currents confer distinct tuning properties that enable neurons to encode the integral or derivative of their input. *Front Cell Neurosci* **8**, 452 (2014).
60. Attwell, D. & Laughlin, S.B. An energy budget for signaling in the grey matter of the brain. *J Cereb Blood Flow Metab* **21**, 1133-1145 (2001).
61. Sengupta, B., Stemmler, M., Laughlin, S.B. & Niven, J.E. Action potential energy efficiency varies among neuron types in vertebrates and invertebrates. *PLoS Comput Biol* **6**, e1000840 (2010).
62. Al-Basha, D. & Prescott, S.A. Intermittent failure of spike propagation in primary afferent neurons during tactile stimulation. *J Neurosci* **39**, 9927-9939 (2019).
63. Speakman, J.R.*, et al.* Set points, settling points and some alternative models: theoretical options to understand how genes and environments combine to regulate body adiposity. *Dis Mod Mech* **4**, 733-745 (2011).
64. O'Leary, T., Williams, A.H., Caplan, J.S. & Marder, E. Correlations in ion channel expression emerge from homeostatic tuning rules. *Proc Natl Acad Sci USA* **110**, E2645-2654 (2013).
65. Aster, R.C., Borchers, B. & Thurber, C.H. *Parameter estimation and inverse problems* (Academic Press, Waltham, MA, 2013).
66. Goldman, M.S., Golowasch, J., Marder, E. & Abbott, L.F. Global structure, robustness, and modulation of neuronal models. *J Neurosci* **21**, 5229-5238 (2001).
67. Soofi, W., Archila, S. & Prinz, A.A. Co-variation of ionic conductances supports phase maintenance in stomatogastric neurons. *J Comput Neurosci* **33**, 77-95 (2012).
68. Hudson, A.E. & Prinz, A.A. Conductance ratios and cellular identity. *PLoS Comput Biol* **6**, e1000838 (2010).
69. Ball, J.M., Franklin, C.C., Tobin, A.E., Schulz, D.J. & Nair, S.S. Coregulation of ion channel conductances preserves output in a computational model of a crustacean cardiac motor neuron. *J Neurosci* **30**, 8637-8649 (2010).
70. Temporal, S., Lett, K.M. & Schulz, D.J. Activity-dependent feedback regulates correlated ion channel mRNA levels in single identified motor neurons. *Curr Biol* **24**, 1899-1904 (2014).
71. Schulz, D.J., Goaillard, J.M. & Marder, E. Variable channel expression in identified single and electrically coupled neurons in different animals. *Nat Neurosci* **9**, 356-362 (2006).
72. Tobin, A.E., Cruz-Bermúdez, N.D., Marder, E. & Schulz, D.J. Correlations in ion channel mRNA in rhythmically active neurons. *PLoS One* **4**, e6742 (2009).
73. Schulz, D.J., Goaillard, J.M. & Marder, E.E. Quantitative expression profiling of identified neurons reveals cell-specific constraints on highly variable levels of gene expression. *Proc Natl Acad Sci USA* **104**, 13187-13191 (2007).

74. Khorkova, O. & Golowasch, J. Neuromodulators, not activity, control coordinated expression of ionic currents. *J Neurosci* **27**, 8709-8718 (2007).
75. Ramocki, M.B. & Zoghbi, H.Y. Failure of neuronal homeostasis results in common neuropsychiatric phenotypes. *Nature* **455**, 912-918 (2008).
76. Gabel, H.W., *et al.* Disruption of DNA-methylation-dependent long gene repression in Rett syndrome. *Nature* **522**, 89-93 (2015).
77. Harnack, D., Pelko, M., Chaillet, A., Chitour, Y. & van Rossum, M.C. Stability of Neuronal Networks with Homeostatic Regulation. *PLoS Comput Biol* **11**, e1004357 (2015).
78. Khubieh, A., Ratté, S., Lankarany, M. & Prescott, S.A. Regulation of cortical dynamic range by background synaptic noise and feedforward inhibition. *Cereb Cortex* **26**, 3357-3369 (2016).
79. Prescott, S.A. & Sejnowski, T.J. Spike-rate coding and spike-time coding are affected oppositely by different adaptation mechanisms. *J Neurosci* **28**, 13649-13661 (2008).
80. Hasenstaub, A., Otte, S., Callaway, E. & Sejnowski, T.J. Metabolic cost as a unifying principle governing neuronal biophysics. *Proc Natl Acad Sci USA* **107**, 12329-12334 (2010).

ACKNOWLEDGEMENTS

This research was funded by a Discovery Grant from the Natural Sciences and Engineering Research Council (NSERC) and by a Foundation Grant from the Canadian Institutes of Health Research (CIHR). H.S. was supported by Ontario Graduate Scholarship, the University of Toronto Centre for the Study of Pain Scholarship, and James F. Crothers Family Scholarship. J.Y. was supported by a SickKids Restracomp Studentship and Ontario Graduate Scholarship. We thank Eve Marder, Etay Hay, Shreejoy Tripathy, and Simon Hardy for constructive feedback on the manuscript.

AUTHOR CONTRIBUTIONS

J.Y., H.S. and S.A.P. conceived and designed the study. J.Y. and H.S. conducted simulations and analyzed data. S.R. conducted experiments. J.Y. and S.A.P. wrote the final paper with feedback from H.S and S.R.

COMPETING INTERESTS

The authors declare no competing interests.

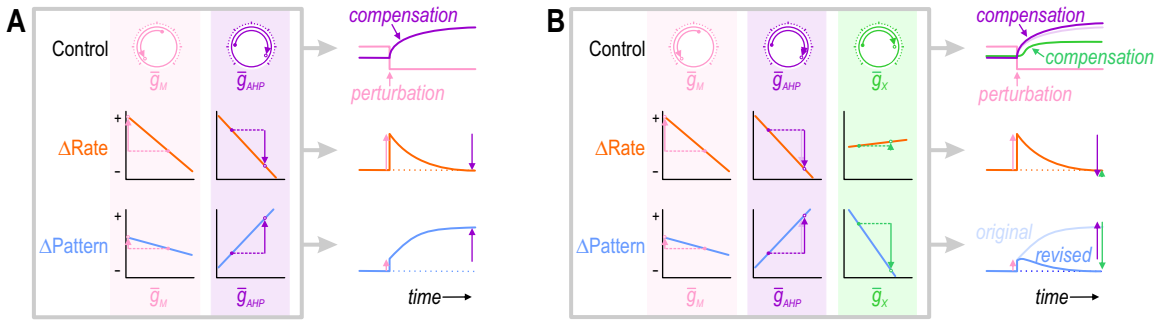

Figure 1. Simultaneous regulation of >1 property in a theoretical neuron. A Challenge. If two ion channels, g_M (pink) and g_{AHP} (purple), both affect firing rate (orange), then the change in firing rate caused by perturbing g_M can be offset by a compensatory change in g_{AHP}. However, if g_M and g_{AHP} also affect firing pattern (blue), but not in exactly the same way, then the compensatory change in g_{AHP} that restores firing rate to its target value may exacerbate rather than resolve the change in firing pattern. **B** Solution. Adjusting g_{AHP} and at least one additional conductance, g_X (green), that affects each property in a different way than g_{AHP}, may enable firing rate and firing pattern to be regulated back to their target values. This suggests that the number of adjustable ion channels ("dials") relative to the number of regulated properties is important. Note that adjusting g_X to restore the firing pattern necessitates a small extra increase in g_{AHP} (compare pale and dark purple); in other words, conductances must be co-adjusted.

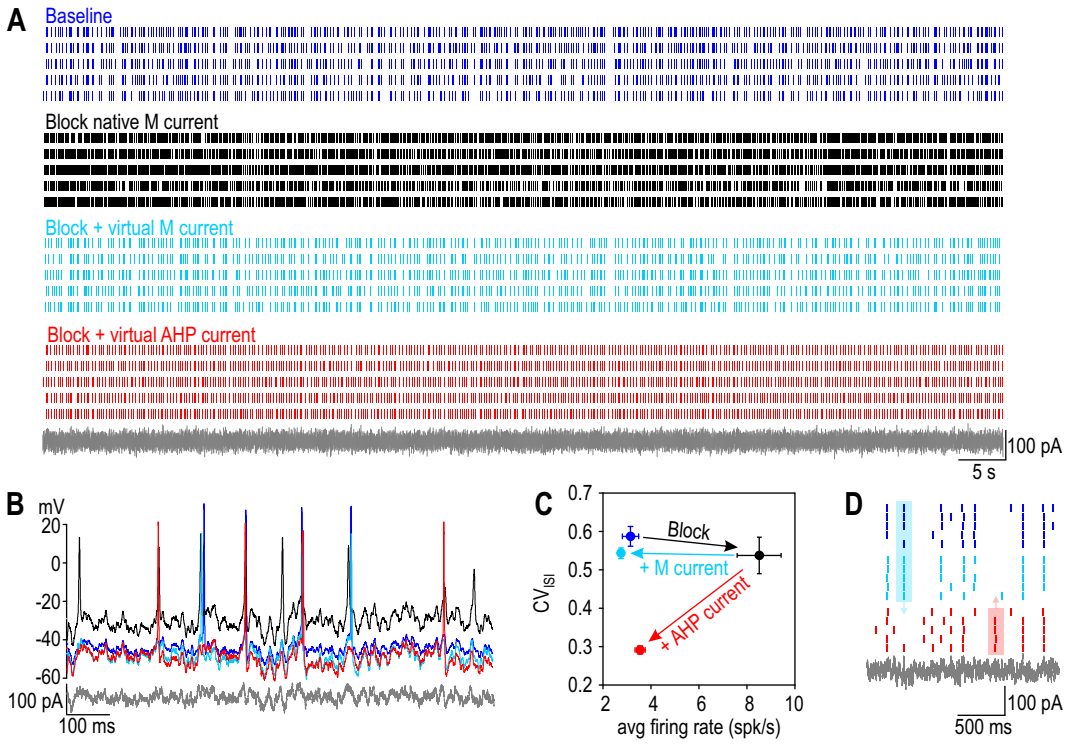

Figure 2. A compensatory change that restores firing rate disrupts firing pattern in a CA1 pyramidal neuron. A Rasters show spiking in a CA1 pyramidal neuron given the same noisy current injection (gray) on five trials under each of four conditions: baseline (blue), after blocking native I_M with 10 μM XE991 (black), and again after inserting virtual I_M (cyan) or virtual I_{AHP} (red) using dynamic clamp. See Methods for virtual conductance parameters. **B** Sample voltage traces under each condition. Blocking I_M caused chronic depolarization and reduced spike heights in addition to increasing the firing rate. Those effects were reversed by inserting virtual I_M or I_{AHP}. **C** Unlike virtual I_M, virtual I_{AHP} made spiking more regular, as reflected in the reduced coefficient of variation of the interspike interval (CV_{ISI}). Data show mean ± SD. **D** Enlarged view of rasters to highlight spikes that occurred with native or virtual I_M but not with virtual I_{AHP} (blue shading) or vice versa (red shading) to illustrate the impact of the change in spike pattern.

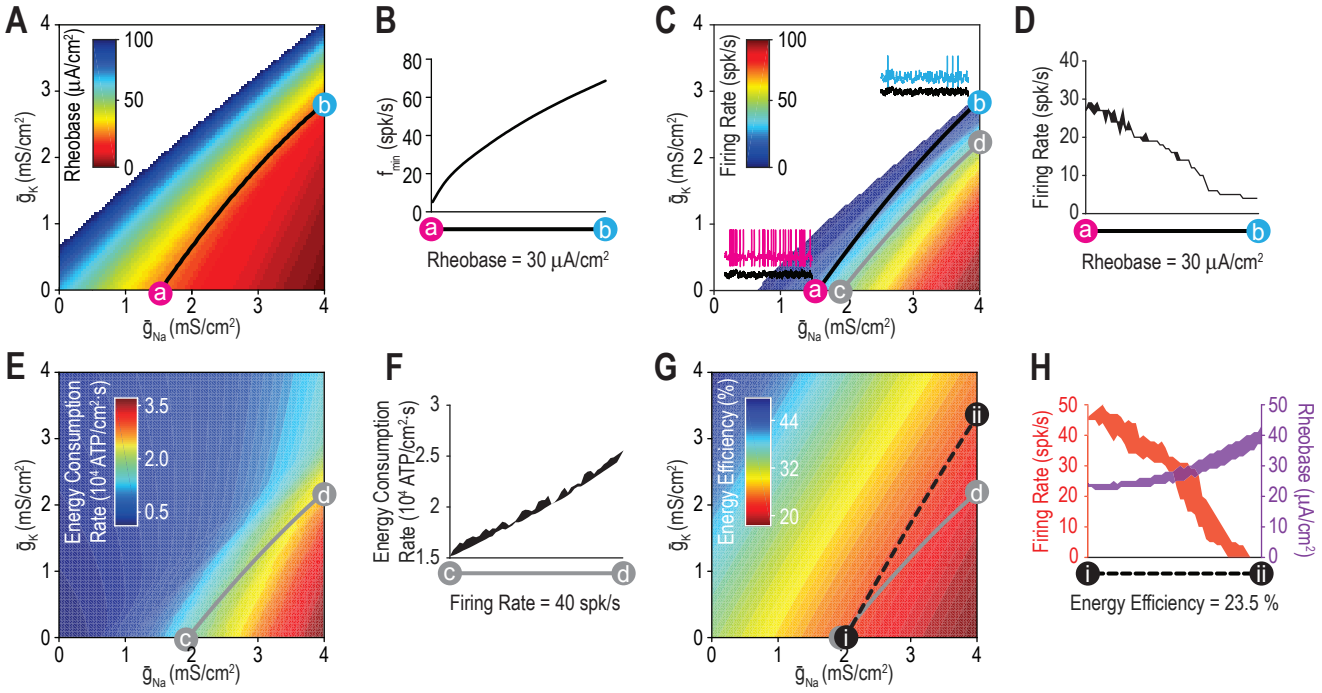

Figure 3. Most ion channel combinations producing the target value for one property produce inconsistent values for other properties. A Color shows the minimum I_{stim} required to evoke repetitive spiking (rheobase) for different combinations of $\bar{g}_{Na}$ and $\bar{g}_K$. Contour linking *a* and *b* highlights density combinations yielding a rheobase of 30 μA/cm². **B** Minimum sustainable firing rate (f_{min}) varied along the iso-rheobase contour. **C** Color shows firing rate evoked by noisy I_{stim} (τ_{stim} = 5 ms, σ_{stim} = 10 μA/cm², μ_{stim} = 40 μA/cm²) for different combinations of $\bar{g}_{Na}$ and $\bar{g}_K$. Adding spike-dependent and -independent forms of adaptation ($\bar{g}_{AHP}$ = 1.75 mS/cm² and $\bar{g}_M$ = 0.5 mS/cm²) broadened the dynamic range. Grey curve shows density combinations yielding a firing rate of 40 spk/s (*i.e.* an iso-firing rate contour; shown in red in **Figs. 4-6**). Insets show sample responses to equivalent noisy stimulation. **D** Firing rate varied along the iso-rheobase contour from panel **A**. **E** Color shows energy consumption rate for different combinations of $\bar{g}_{Na}$ and $\bar{g}_K$ based on firing rates shown in panel **C**. Iso-firing rate contour *c-d* (grey line in panel **C**) does not align with energy contours. ATP consumed by the Na^+/K^+ pump was calculated from the total Na^+ influx and K^+ efflux determined from the corresponding currents. **F** Energy consumption rate varied along the iso-firing rate contour. **G** Color shows energy efficiency per spike for different combinations of $\bar{g}_{Na}$ and $\bar{g}_K$. Energy efficiency was calculated as the capacitive minimum C·ΔV divided by total Na^+ influx, where C is capacitance and ΔV is spike amplitude (see **Fig. 3 - figure supplement 2**). Density combinations along contour *i-ii* (dashed line) yield energy efficiency of 23.5% (shown in green in **Fig. 5**). **H** Both rheobase and firing rate varied along the iso-energy efficiency contour.

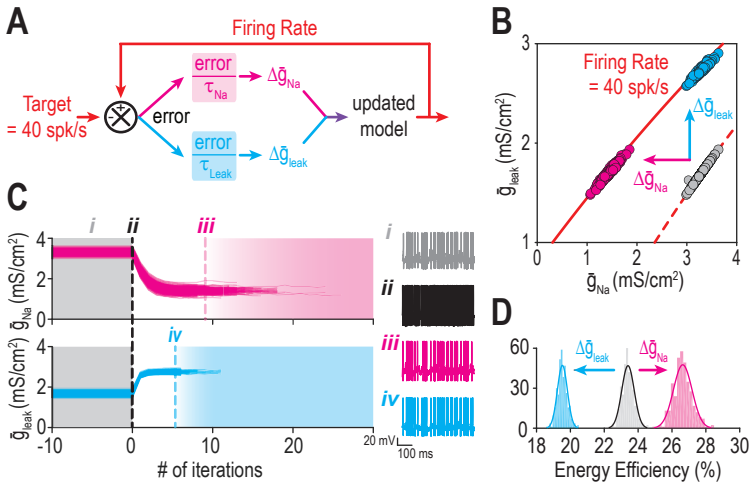

Figure 4. Ion channel changes mediating the same effect on firing rate can oppositely affect energy efficiency.
A Schematic shows how a difference in firing rate from its target value creates an error that is reduced by updating $\bar{g}_{Na}$ or $\bar{g}_{leak}$.
B Iso-firing rate contours for 40 spk/s are shown for different combinations of $\bar{g}_{Na}$ and $\bar{g}_{leak}$ with $\bar{g}_K$ at baseline (2 mS/cm^2, dashed red curve) and after $\bar{g}_K$ was "knocked out" (0 mS/cm^2, solid red curve). When $\bar{g}_K$ was abruptly reduced, starting models (grey dots) spiked rapidly (~93 spk/s) before firing rate was regulated back to its target value by compensatory changes in either $\bar{g}_{Na}$ (pink) or $\bar{g}_{leak}$ (cyan). Models evolved in different directions and settled at different positions along the solid curve. **C** Trajectories show evolution of $\bar{g}_{Na}$ and $\bar{g}_{leak}$. Trajectories are terminated once target firing rate is reached. Sample traces show responses before (grey) and immediately after (black) $\bar{g}_K$ was reduced, and again after compensatory changes in $\bar{g}_{Na}$(pink) or $\bar{g}_{leak}$(cyan). **D** Distributions of energy efficiency are shown before (grey) and after firing rate regulation via control of $\bar{g}_{Na}$ (pink) or $\bar{g}_{leak}$ (cyan).

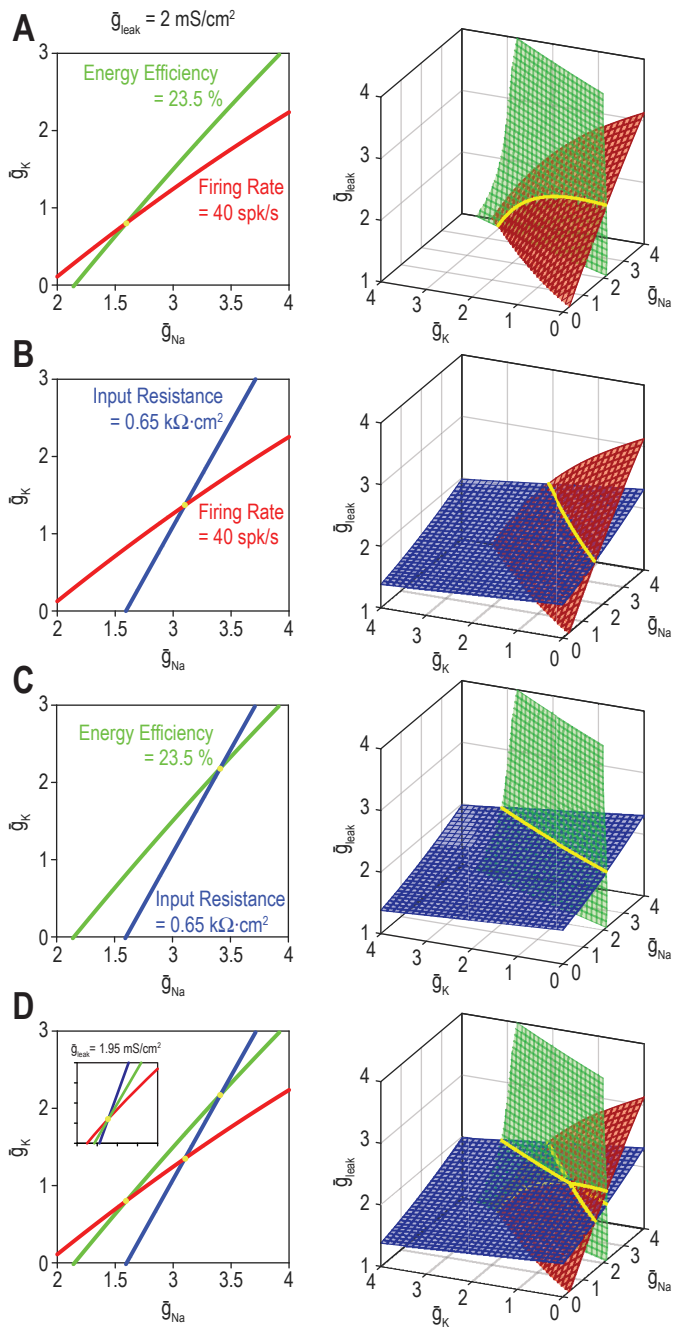

Figure 5. A degenerate solution for *n* properties requires at least *n* + 1 controllable ion channels. Curves on left depict single-output solutions sets based on control of $\bar{g}_{Na}$ and $\bar{g}_K$ (n_{in} = 2). Surfaces on right depict single-output solution sets based on control of $\bar{g}_{Na}$, $\bar{g}_K$, and $\bar{g}_{leak}$ (n_{in} = 3). Intersection (yellow) of single-output solutions at a point constitutes a unique multi-output soluion, whereas intersection along a curve (or higher-dimensional manifold) constitutes a degenerate multi-output solution. **A** Curves for firing rate (40 spk/s) and energy efficiency (23.5%) intersect at a point whereas the corresponding surfaces intersect along a curve. Solutions for firing rate and input resistance (0.65 kΩ·cm2) (**B**) and for energy efficiency and input resistance (**C**) follow the same pattern as in **A**. **D** For n_{in} = 2 (left), curves for firing rate, energy efficiency and input resistance do not intersect at a common point unless $\bar{g}_{leak}$ is reset to 1.95 mS/cm² (inset). For n_{in} = 3 (right), the three surfaces intersect at the same point as in the inset.

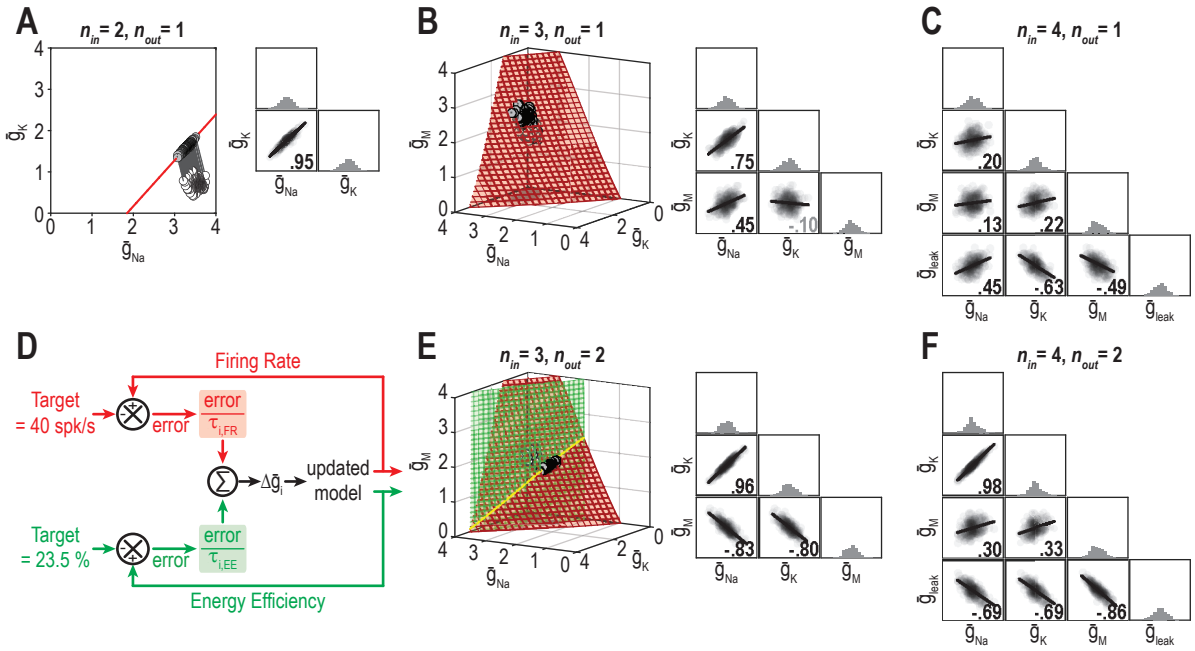

Figure 6. The dimensionality of solution space affects ion channel correlations. A Starting from a normally distributed cluster of $\bar{g}_{Na}$ and $\bar{g}_K$ (white dots) yielding an average firing rate of 73 spk/s, $\bar{g}_{Na}$ and $\bar{g}_K$ (n_{in} = 2) were homeostatically adjusted to regulate firing rate (n_{out} = 1) to its target value of 40 spk/s. Grey lines show trajectories. Because solutions (grey dots) converge on a curve, the pairwise correlation between $\bar{g}_{Na}$ and $\bar{g}_K$ is predictably strong. Scatterplots show solutions centered on the mean and normalized by the standard deviation (z-scores). Correlation coefficient (R) is shown in the bottom right corner of each scatter plot. **B** Same as **A** (n_{out} = 1) but via control of $\bar{g}_{Na}$, $\bar{g}_K$ and $\bar{g}_M$ (n_{in} = 3). Homeostatically found solutions converge on a surface and ion channel correlations are thus weaker. **C** If $\bar{g}_{leak}$ is also controlled (n_{in} = 4), solutions converge on a hard-to-visualize volume (not shown) and pairwise correlations are further weakened. **D** Schematic shows how errors for two regulated properties are combined: the error for each property is calculated separately and is scaled by its respective control rate τ to calculate updates, and all updates for a given ion channel (*i.e.* originating from each error signal) are summed. **E** Same as **B** (n_{in} = 3), but for regulation of firing rate and energy efficiency (n_{out} = 2). Homeostatically found solutions once again converge on a curve (yellow), which now corresponds to the intersection of two surfaces; ion channel correlations are thus strong, like in **A**. **F** If n_{in} is increased to 4 while n_{out} remains at 2, solutions converge on a surface (not shown) and ion channel correlations weaken.

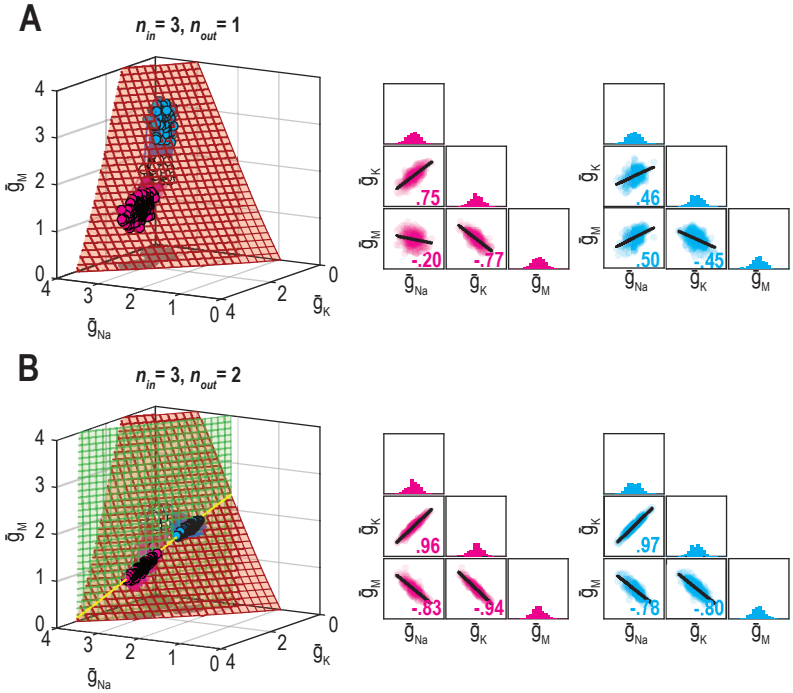

Figure 7. The dimensionality of solution space and relative control rates shape ion channel correlations. A Homeostatic regulation of firing rate via control of $\bar{g}_{Na}$, $\bar{g}_K$ and $\bar{g}_M$. Same as **Figure 6B**, but for two new sets of control rates (see **Table S1**). Solutions found for each set of rates (pink and cyan) approached the surface from different angles and converged on the surface with different patterns, thus producing distinct ion channel correlations (consistent with O'leary et al.[64]). **B** Same as **A** (n_{in} = 3), but for homeostatic regulation of firing rate and energy efficiency (n_{out} = 2). Solutions converge on a curve (yellow), giving rise to virtually identical ion channel correlations regardless of control rates.

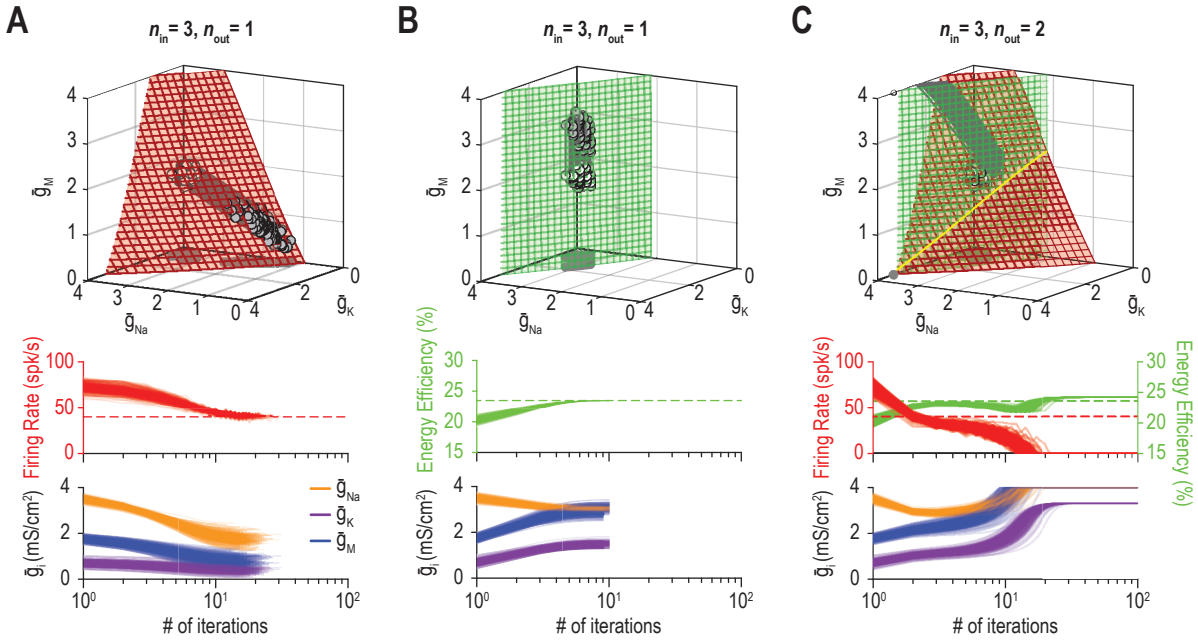

Figure 8. Low-dimensional solutions can be hard for homeostatic regulation to "find". A Homeostatic regulation of firing rate (n_{out} = 1) via control of $\bar{g}_{Na}$, $\bar{g}_K$ and $\bar{g}_M$ (n_{in} = 3), like in **Figures 6B** and **7A** but using a different set of control rates (see **Table S1**). Solutions converged onto the iso-firing rate surface (top panel) and firing rate was regulated to its target value in <30 iterations (bottom panel). **B** Same as **A** (n_{in} = 3) but for homeostatic regulation of energy efficiency (n_{out} = 1). Solutions converged on the iso-energy efficiency surface (top panel) and energy efficiency was regulated to its target value in ~10 iterations (bottom panel). **C** Homeostatic regulation of firing rate and energy efficiency (n_{out} = 2) via control of the same ion channels (n_{in} = 3) using the same relative rates and initial values as in **A** and **B**. Neither firing rate (red trajectories) nor energy efficiency (green trajectories) reached its target value. Conductance densities were capped at 4 mS/cm^2 but this does not account for trajectories not reaching their target.

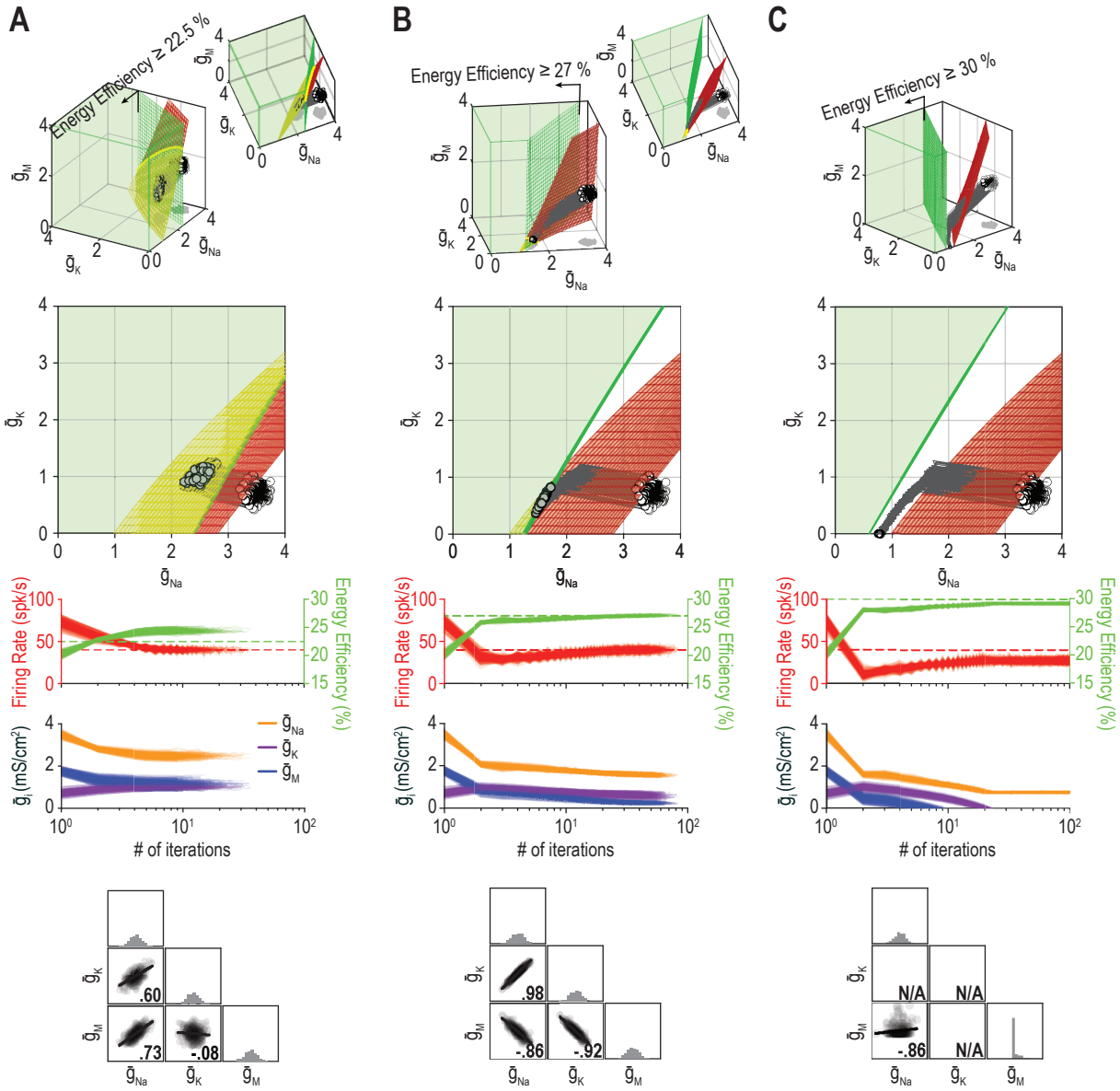

Figure 9. The outcome of homeostatic regulation depends on if and how single-output solutions sets intersect. Homeostatic regulation of firing rate and energy efficiency (n_{out} = 2) via control of $\bar{g}_{Na}$, $\bar{g}_K$ and $\bar{g}_M$ (n_{in} = 3). For these simulations, energy efficiency was maintained above a lower bound rather than being regulated to a specific target value; accordingly, the single-output solution set for energy efficiency corresponds to a volume (green) rather than a surface. **A** For energy efficiency ≥22%, homeostatically determined solutions converge on the iso-firing rate surface (red) in a region sitting within the green volume (top panel). The rate of convergence and resulting ion channel correlations are shown in the middle and bottom panels, respectively. **B** For energy efficiency ≥27%, solutions initially converge on the red surface in a region outside the green volume, but trajectories then bend and proceed across the red surface until that surface reaches the green volume. Because solutions converge on a curve, ion channel correlations are stronger than in **A**, where solutions distributed across a surface. **C** For energy efficiency ≥30%, the red surface and green volume do not intersect. Consequently, solutions settle between the two single-output solution sets (top panel) without either property reaching its target (middle panel). The outcome represents the balance achieved by the opposing pull of control mechanisms regulating different properties, and depends entirely on $\bar{g}_{Na}$ since $\bar{g}_K$ and $\bar{g}_M$ cannot become negative (bottom panel).